


 Cite this: *RSC Adv.*, 2023, **13**, 12781

## Metal organic framework derived $\text{NiO}_x$ nanoparticles for application as a hole transport layer in perovskite solar cells

Md. Ariful Islam,<sup>a</sup> Vidhya Selvanathan,<sup>\*f</sup> Puvaneswaran Chelvanathan,<sup>a</sup> M. Mottakin,<sup>ab</sup> Mohammad Aminuzzaman,<sup>c</sup> Mohd Adib Ibrahim,<sup>ID a</sup> Ghulam Muhammad<sup>ID d</sup> and Md. Akhtaruzzaman<sup>ID \*ae</sup>

$\text{NiO}_x$  as a hole transport layer (HTL) has gained a lot of research interest in perovskite solar cells (PSCs), owing to its high optical transmittance, high power conversion efficiency, wide band-gap and ease of fabrication. In this work, four different nickel based-metal organic frameworks (MOFs) using 1,3,5-benzenetricarboxylic acid (BTC), terephthalic acid (TPA), 2-aminoterephthalic acid (ATPA), and 2,5-dihydroxyterephthalic acid (DHTPA) ligands respectively, have been employed as precursors to synthesize  $\text{NiO}_x$  NPs. The employment of different ligands was found to result in  $\text{NiO}_x$  NPs with different structural, optical and morphological properties. The impact of calcination temperatures of the MOFs was also studied and according to field emission scanning electron microscopy (FESEM), all MOF-derived  $\text{NiO}_x$  NPs exhibited lower particle size at lower calcination temperature. Upon optimization, Ni-TPA MOF derived  $\text{NiO}_x$  NPs calcined at 600 °C were identified to be the best for hole transport layer application. To explore the photovoltaic performance, these  $\text{NiO}_x$  NPs have been fabricated as a thin film and its structural, optical and electrical characteristics were analyzed. According to the findings, the band energy gap ( $E_g$ ) of the fabricated thin film has been found to be 3.25 eV and the carrier concentration, hole mobility and resistivity were also measured to be  $6.8 \times 10^{14} \text{ cm}^{-3}$ ;  $4.7 \times 10^{14} \Omega \text{ cm}$  and  $2.0 \text{ cm}^2 \text{ V}^{-1} \text{ s}^{-1}$ , respectively. Finally, a numerical simulation was conducted using SCAPS-1D incorporating the optical and electrical parameters from the thin film analysis. FTO/TiO<sub>2</sub>/CsPbBr<sub>3</sub>/ $\text{NiO}_x$ /C has been utilized as the device configuration which recorded an efficiency of 13.9% with  $V_{oc}$  of 1.89 V,  $J_{sc}$  of 11.07 mA cm<sup>-2</sup>, and FF of 66.6%.

Received 3rd April 2023  
 Accepted 12th April 2023

DOI: 10.1039/d3ra02181e  
[rsc.li/rsc-advances](http://rsc.li/rsc-advances)

## 1 Introduction

Metal oxide nanostructures possess numerous unique features that become distinct from those present in the bulk solid state due to their size differences. Particle size reduction in the nanoscale domain offers a variety of unique characteristics, including low sintering temperature, large specific surface area and quantum size effect.<sup>1</sup> Out of all the metal oxides,  $\text{NiO}_x$

nano-structures have received substantial scientific interest owing to their high band gaps (3.6–4.0 eV) and p-type electrical conductivity characteristics.<sup>2</sup> Moreover,  $\text{NiO}_x$  nanoparticles (NPs) offer a number of applications including in battery cathodes,<sup>3</sup> as catalysis,<sup>4</sup> electrodes of fuel cells, in the field of electrochromic films,<sup>5</sup> gas sensors<sup>6</sup> and magnetic materials.<sup>7</sup> Additionally,  $\text{NiO}_x$  NPs are also being used in smart windows,<sup>8</sup> as the effective hole transporting layer (HTL) in PSCs,<sup>9</sup> dye-sensitized photocathodes<sup>10</sup> and electrochemical supercapacitors.<sup>11</sup> As a hole transport layer (HTL),  $\text{NiO}_x$  is very promising for PSCs because of its deep valence band, affordable cost, high optical transmittance and outstanding stability.<sup>12,13</sup> Recently, a number of experiments have been conducted on  $\text{NiO}_x$ -based PSCs to make the device more reliable and efficient. In order to generate a uniform and homogenous thin film, Pei-Huan Lee *et al.* conducted an emulsion process to synthesize  $\text{NiO}_x$  NPs. Using this thin film, they achieved a PCE of 18%.<sup>13</sup> Shuangjie Wang *et al.* applied an ionic liquid ( $\text{NiO}_x$ -IL) during the synthesis process and they found a promising PCE of 22.62%.<sup>14</sup> The structural, electrical, optical, compositional and magnetic properties of  $\text{NiO}_x$  NPs are highly dependent on the

<sup>a</sup>Solar Energy Research Institute (SERI), Universiti Kebangsaan Malaysia (UKM), 43600 Bangi, Selangor, Malaysia. E-mail: akhtar@ukm.edu.my

<sup>b</sup>Department of Applied Chemistry and Chemical Engineering, Bangabandhu Sheikh Mujibur Rahman Science and Technology University, Gopalganj-8100, Bangladesh

<sup>c</sup>Department of Chemical Science, Faculty of Science, Universiti Tunku Abdul Rahman (UTAR), Perak Campus, Jalan Universiti, Bandar Barat, 31900 Kampar, Perak D. R., Malaysia

<sup>d</sup>Department of Computer Engineering, College of Computer and Information Sciences, King Saud University, Riyadh, Saudi Arabia

<sup>e</sup>Graduate School of Pure and Applied Sciences, University of Tsukuba, Tsukuba, Ibaraki 305-8573, Japan

<sup>f</sup>Institute of Sustainable Energy, Universiti Tenaga Nasional (The Energy University), Jalan Ikram-Uniten, Kajang 43000, Selangor, Malaysia



synthesis process, particle size and shape. Generally, the experimental route adopted for the synthesis of  $\text{NiO}_x$  NPs is very crucial in governing a number of key factors, including crystallinity, size and shape, composition-purity of the final product.<sup>15</sup> So far, in comparison to other conventional methods like spray-pyrolysis, co-precipitation, sol-gel, microwave pyrolysis, thermal decomposition; solvothermal is an efficient and simple technique for the synthesis of NPs because it offers comparatively large specific surface area with low temperature processing step.<sup>16</sup> Solvothermal technique has successfully overcome challenges such as utilization of expensive specialized equipment, low energy usage, high purity and large-scale manufacturing.<sup>16</sup> Considering all of these, much effort has been devoted in recent past to the development of metal-organic frameworks (MOFs) as precursors utilized in the synthesis process of porous oxides. Basically, MOFs are defined as porous hybrid compound, that consist of metal ions which are connected with organic ligands *via* coordination bond and create a three-dimensional framework.<sup>17,18</sup> In comparison, MOFs offer a wider range of options to design and construct the hierarchically nanostructures, a class of polyfunctional compounds with a number of morphological and topological characteristics.<sup>19</sup>

Most studies have stated that the morphology and size of particles of the metal oxides derived from MOF depends on the chemical structure of the ligand used which in turn, tunes the overall architecture. Typically for any NP synthesis, the homogeneity, NPs shape and size can be tuned by changing the solution concentration, pH, nucleation rate, reaction temperature and presence of complexing agent in the synthesis process.<sup>20</sup> Among these factors, calcination temperature is very important because it alters the shape and morphological properties of nanoparticles as well as creating defects, which leads to the formation of new energy state.<sup>21</sup> The phase of the materials is often influenced by the sintering temperature, which in turn affects the materials' structural and optical properties.<sup>21</sup> So, its highly necessary to calcine the produced nanoparticles at elevated temperatures in order to obtain single phase nanostructures of the right size.<sup>20</sup> The removal of impure phases, and an improvement in particle density and a rise in crystallites are some potential benefits of this step.<sup>20</sup> For synthesis of MOF derived NPs, it is essential to ensure the calcination temperature is high enough to produce high purity metal oxides while at the same time ensure particles with desired size and shape is produced.

This article addressed the synthesis process of  $\text{NiO}_x$  NPs derived from metal-organic framework by utilizing four distinct ligands namely 1,3,5-benzenetricarboxylic acid (**BTC**), terephthalic acid (**TPA**), 2-aminoterephthalic acid (**ATPA**), 2,5-dihydroxyterephthalic acid (**DHTPA**). The effect of different ligand structure of the MOF precursors calcined at different temperature on the structural, morphological and optical properties of the synthesized  $\text{NiO}_x$  NPs was analyzed. In extension the MOF derived NPs were applied as potential hole transport layer (HTL) in n-i-p PSCs to elucidate the future potential as component in energy storage devices.

## 2 Materials and methods

### 2.1 Materials

All chemicals and reagents were utilized, without additional purification.  $\text{Ni}(\text{NO}_3)_2 \cdot 6\text{H}_2\text{O}$ ; 1,3,5-benzenetricarboxylic acid (**BTC**), terephthalic acid (**TPA**), 2-aminoterephthalic acid (**ATPA**), 2,5-dihydroxyterephthalic acid (**DHTPA**), dimethylformamide (DMF), ethanol, KOH, methanol, acetone, absolute ethanol (99.9%), acetic acid, ethylene glycol, 1-ethyl-3-methylimidazolium tetrafluoroborate, fluorine doped tin oxide (FTO) coated soda-lime glass substrate (SLG), were pursued from Sigma Aldrich, Germany.

### 2.2 Synthesis of MOF derived $\text{NiO}_x$ NPs

The MOF-derived  $\text{NiO}_x$  NPs were synthesized by solvothermal method (Fig. 1). For this experiment, 2.1 mmol  $\text{Ni}(\text{NO}_3)_2 \cdot 6\text{H}_2\text{O}$  and 3 mmol ligand (**BTC/TPA/ATPA/DHTPA**) were well dispersed in 15 mL dimethylformamide (DMF). The resulting dispersed solutions were placed in 100 mL Teflon-polytetrafluoroethylene coated autoclave with stainless steel jacket at 160 °C for 12 h. After completing the reaction, the colloidal solutions were taken out from autoclave and left it for cooling down to ambient temperature naturally. After centrifuging the colloidal solution, it was repeatedly rinsed with ethanol and water for 3 times. Then the colloidal solutions were centrifuged and rinsed with ethanol and water for several time. The products were dried in an oven at 80 °C for 8 h to obtain MOFs. Finally, these Ni-MOFs were calcined in a furnace for 5 hours at different temperature (600 °C, 700 °C, and 900 °C) to achieve the desired  $\text{NiO}_x$  nanoparticles.

### 2.3 Fabrication of $\text{NiO}_x$ thin film

Bare SLG and FTO coated SLG were used as a substrate for the deposition of  $\text{NiO}_x$  thin films. Bare SLG has been utilized to measure the thin film's electrical characteristics, while FTO coated SLG was used to evaluate the film's structural and optical characteristics. The substrates were cleaned by using an ultrasonic cleaner with ethanol, acetone, and DI water; afterwards dried with a stream of  $\text{N}_2$  gas. Prior to spin coating, all substrates were treated for 15 min with UV-ozone plasma.  $\text{NiO}_x$  colloidal dispersion was prepared by dissolving 40 mg  $\text{NiO}_x$  synthesized powder into 2 mL absolute ethanol with the concentration of 20 mg mL<sup>-1</sup> 30  $\mu\text{L}$  acetic acid, 150  $\mu\text{L}$  ethylene glycol and 500  $\mu\text{L}$  ionic liquid ( $\text{BMIMBF}_4$ ) have also been incorporated to make a homogenous dispersion. The dispersion was subsequently coated onto the glass substrate with the speed of 4000 rpm for 30 s, followed by 10 min of baking at 200 °C on a hot plate. Finally, the films calcined at 300 °C for 1 h into a furnace. All of these operations were performed under ambient conditions.

### 2.4 Nanoparticles and thin film characterization

The morphological and structural characteristics of MOF-derived  $\text{NiO}_x$  NPs and thin film were carried out by using several characterization approaches such as X-ray diffraction



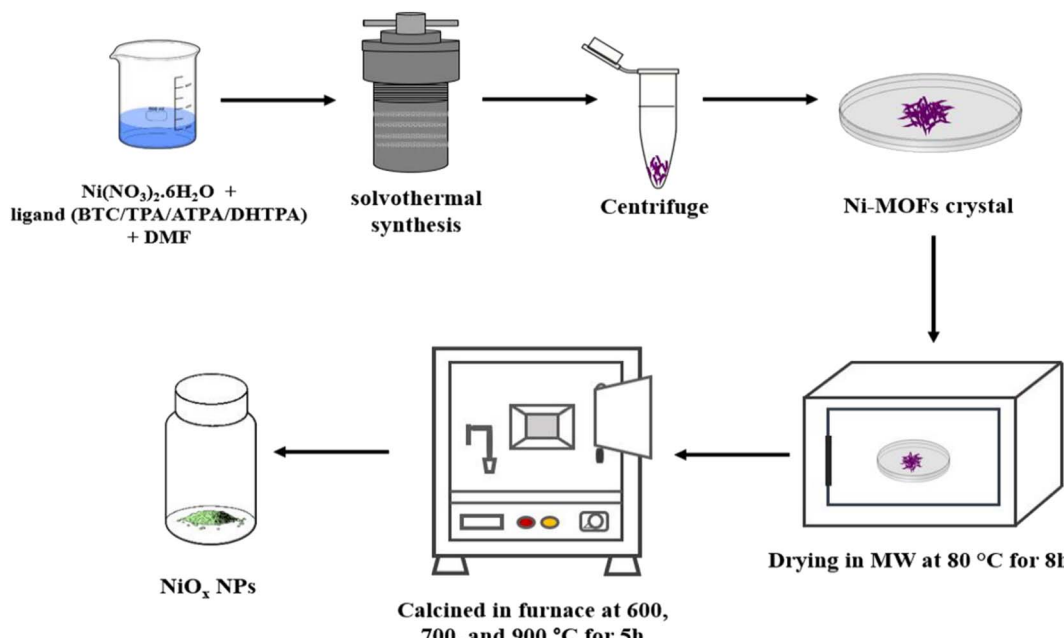


Fig. 1 Synthesis process of MOF-derived  $\text{NiO}_x$  NPs.

(XRD), field emission scanning electron microscope (FeSEM), absorption spectra (UV-Vis) coupled with Fourier transform infrared (FTIR). The XRD were measured in the  $2\theta$  with a region of  $10^\circ$  to  $90^\circ$  for NPs and  $10^\circ$  to  $80^\circ$  for thin film respectively utilizing an X-ray diffractometer 'BRUKER aXS-D8 Advance Cu-K $\alpha$ '. For the detection of functional group, Bruker FTIR spectrometer has been used with spectral range from 4000 to 500  $\text{cm}^{-1}$ . To investigate the grain size, surface morphology and growth of NPs FeSEM model 'LEO 1450 VP' was utilized. UV-Vis spectrophotometer PerkinElmer Lambda 35 was being used to evaluate optoelectronic characteristics, including optical absorbance and transmittance. The electrical characteristics of thin film were measured, using the HMS ECOPIA 3000 Hall effect measuring system under a magnetic field (0.57 T).

### 3 Results and discussion

#### 3.1 Properties of MOF derived $\text{NiO}_x$ nanoparticle

**3.1.1 Structural properties.** Fig. 2 depicts the XRD pattern of  $\text{NiO}_x$  NPs obtained from MOFs employing four different ligand following calcination at 600 °C, 700 °C, and 900 °C. It has been revealed that, all of the  $\text{NiO}_x$  NPs sample showed five major diffraction intensity at  $2\theta$  with the values of 37.2°, 43.2°, 62.8°, 75.4°, and 79.4°, were exactly indexed as the cubic structure's crystallographic plane of (111), (200), (220), (311), and (222) [JCPDS, No. 04-0835], which is in excellent agreement with previous diffractogram values of  $\text{NiO}_x$ .<sup>22,23</sup> A noticeable peak intensities variation was also evident among the sample, when sintered at 600 °C and 700 °C and 900 °C. The degree of crystallinity of NPs reduced at lower calcination temperature because, at lower heat treatment certain carbon residues still remain in the synthesized powder.

Highly pure  $\text{NiO}_x$  can be obtained with high sintering temperature (900 °C), result in sharp peak intensity.  $\text{NiO}_x$ -BTC (700 °C);  $\text{NiO}_x$ -ATPA (600 °C and 700 °C); and  $\text{NiO}_x$ -DHTPA (600 °C), all exhibit two faint peaks at  $2\theta$  with the value of around

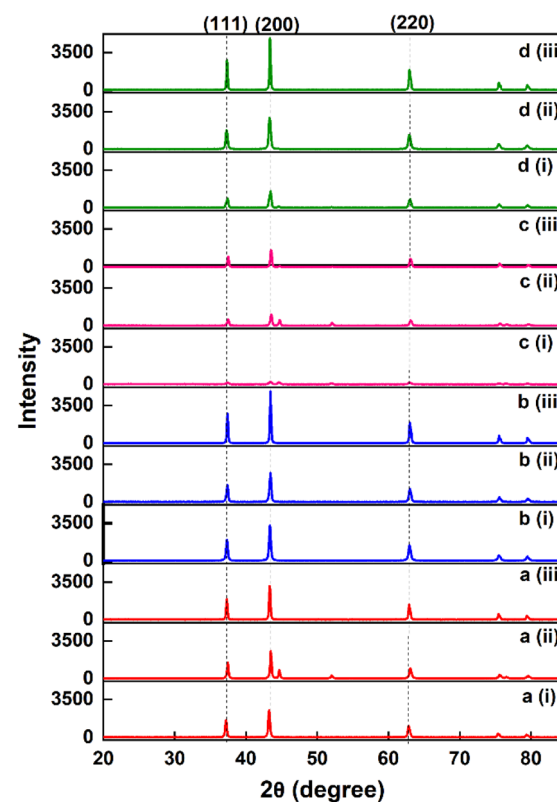


Fig. 2 X-ray diffractogram of MOF-derived  $\text{NiO}_x$  nanoparticles (a)  $\text{NiO}_x$ -BTC (b)  $\text{NiO}_x$ -TPA (c)  $\text{NiO}_x$ -ATPA and (d)  $\text{NiO}_x$ -DHTPA mediated calcined at (i) 600 °C and (ii) 700 °C (iii) 900 °C.



Table 1 Average crystallite size and strain of  $\text{NiO}_x$  NPs with different calcination temperature

Material	Calcination temperature (°C)	Average crystallite size (nm)	Average strain (ε)
$\text{NiO}_x$ -BTC	600	24.77	0.0029
	700	25.69	0.0029
	900	29.54	0.0025
$\text{NiO}_x$ -TPA	600	23.79	0.0030
	700	24.34	0.0030
	900	30.81	0.0023
$\text{NiO}_x$ -ATPA	600	20.60	0.0037
	700	22.20	0.0027
	900	28.03	0.0026
$\text{NiO}_x$ -DHTPA	600	21.90	0.0033
	700	22.27	0.0033
	900	31.39	0.0023

44.8° and 51.7° due to impurities in the synthesized powder. With the help of Scherer's formula, the average crystal sizes ( $D$ ) were determined.<sup>24</sup>

$$D = \frac{0.94\lambda}{\beta \cos \theta} \quad (1)$$

where,  $D$  is the average (Avg) crystallite size;  $\beta$  is the FWHM width of the diffraction peak;  $\lambda$  is the wavelength X-ray; and  $\theta$  is the diffraction angle.

Table 1 shows that crystallite size increases along with a rise in sintering temperature. At higher heat treatment, particles imperfections, edges and flaws are removed, resulting in large size crystallites with definite crystalline phase.<sup>25</sup>

Furthermore, peak stretching or broadening is relayed to the quantum confinement and lattice strain effect of NPs because of its large crystallite size and grain boundaries, respectively. To investigate the influence of strain on the structural characteristics of  $\text{NiO}_x$  nanoparticles, Williamson Hall (W-H) analysis is introduced. The W-H equation is represented as<sup>26</sup>

$$\beta \cos \theta = \frac{K\lambda}{D} + 4\epsilon \sin \theta \quad (2)$$

where,  $\beta$  is the FWHM width of the diffraction peak obtained at particular angle  $\theta$ ,  $D$  is the average crystallite size;  $\theta$  is the diffraction angle;  $K$  is the shape factor with the value of 0.9;  $\lambda$  is the wavelength of the X-ray and  $\epsilon$  is crystallite strain.

Table 1 further demonstrates the relation between strain and crystallite size of  $\text{NiO}_x$  NPs. It has been observed that the strain reduces as the size of the crystallites increase. The reason for this behavior is the possibility of impurities and defects in NPs and also the surface area is vast in contrast.<sup>26</sup> Therefore, XRD indicates that  $\text{NiO}_x$ -TPA (900 °C) and  $\text{NiO}_x$ -DHTPA (900 °C) has the least strain value approximately 0.0023, compared to other NPs, indicating that they are highly crystalline with less structural flaws.

Fig. 3 illustrates the FTIR absorption spectra of all synthesized Ni-MOFs and their corresponding NPs. FTIR study of Ni-BTC MOF has been described in Fig. 3a. The formation of Ni-BTC MOFs has been confirmed by obtaining a significant shift in the carbonyl (−CO−) groups at 1608 cm<sup>−1</sup>, suggesting that the ligand's carboxylate moieties have been deprotonated

and coordinated with  $\text{Ni}^{2+}$ . Moreover, the Ni–O stretching vibration is characterized by a strong absorption spectrum at 724 cm<sup>−1</sup>. O–H stretching was found as a wideband at 2800–3500 cm<sup>−1</sup>, suggesting the coordinated water molecule in Ni-BTC MOF prior to activation.<sup>27</sup> Fig. 3b depicts the FT-IR spectra of the Ni-TPA metal–organic framework. As shown in Fig. 3b, Ni-TPA MOF exhibits two prominent peaks at around 1380 cm<sup>−1</sup> and 1580 cm<sup>−1</sup> accordingly, which are due to the symmetric and asymmetric stretching of ligand's carboxyl (−COO<sup>−</sup>) group. Separating the stretching modes indicated that TPA ligand's −COOH groups were linked to  $\text{Ni}^{2+}$  ions through a bidentate binding manner.<sup>28</sup> Narrow and weak bands at 1025 cm<sup>−1</sup> is owing to the stretching (C–H) and bending (C–H) of aromatic ring, which indicating the presence of organic ligand in the MOF. The wide peaks in between 3400–3600 cm<sup>−1</sup> may be attributed owing to acidic −OH or crystal water.<sup>29</sup> Investigation of the FTIR spectra of Ni-ATPA MOF as shown in Fig. 3c, indicating −NH<sub>2</sub> stretching vibration at around 3308 cm<sup>−1</sup>. The absorption peaks at around 1387–1689 cm<sup>−1</sup> may be detected owing to symmetric and asymmetric stretching vibrations of the −COOH groups. Moreover, O–Ni–O vibrational peaks had been found at 530 cm<sup>−1</sup> and 668 cm<sup>−1</sup> in respective Ni-ATPA MOF, indicating the establishment of the coordination bonding among the −COOH groups from ATPA and  $\text{Ni}^{2+}$ .<sup>30</sup> For the Ni-DHTPA, the benzene rings out-of-plane vibrational peak detected at around 888 cm<sup>−1</sup> (Fig. 3d). For carboxylate groups, symmetric and asymmetric stretching appears at around 1410 cm<sup>−1</sup> and 1556 cm<sup>−1</sup>. The interlayer water and C–O–H contribute to the wide band at 3425 cm<sup>−1</sup>. This implies that  $\text{Ni}^{2+}$  has been effectively coordinated with DHTPA ligand.<sup>31,32</sup>

In respect of FTIR spectra study, all  $\text{NiO}_x$ -MOF derived NPs showed the absorption in similar region and there were no traces of peaks attributed to ligands in the MOF. This observation verifies that the Ni-MOF structures were completely transformed into  $\text{NiO}_x$  upon calcination even at 600 °C. It has been observed that, O–Ni–O vibrations are responsible for the FTIR spectrum peak about 663 and 443 cm<sup>−1</sup>. Furthermore, the wide peak at 1398, 3422 and 1622 cm<sup>−1</sup> can be ascribed to stretching and bending vibration of the hydroxyl group captured on the surface of the catalyst from the environment



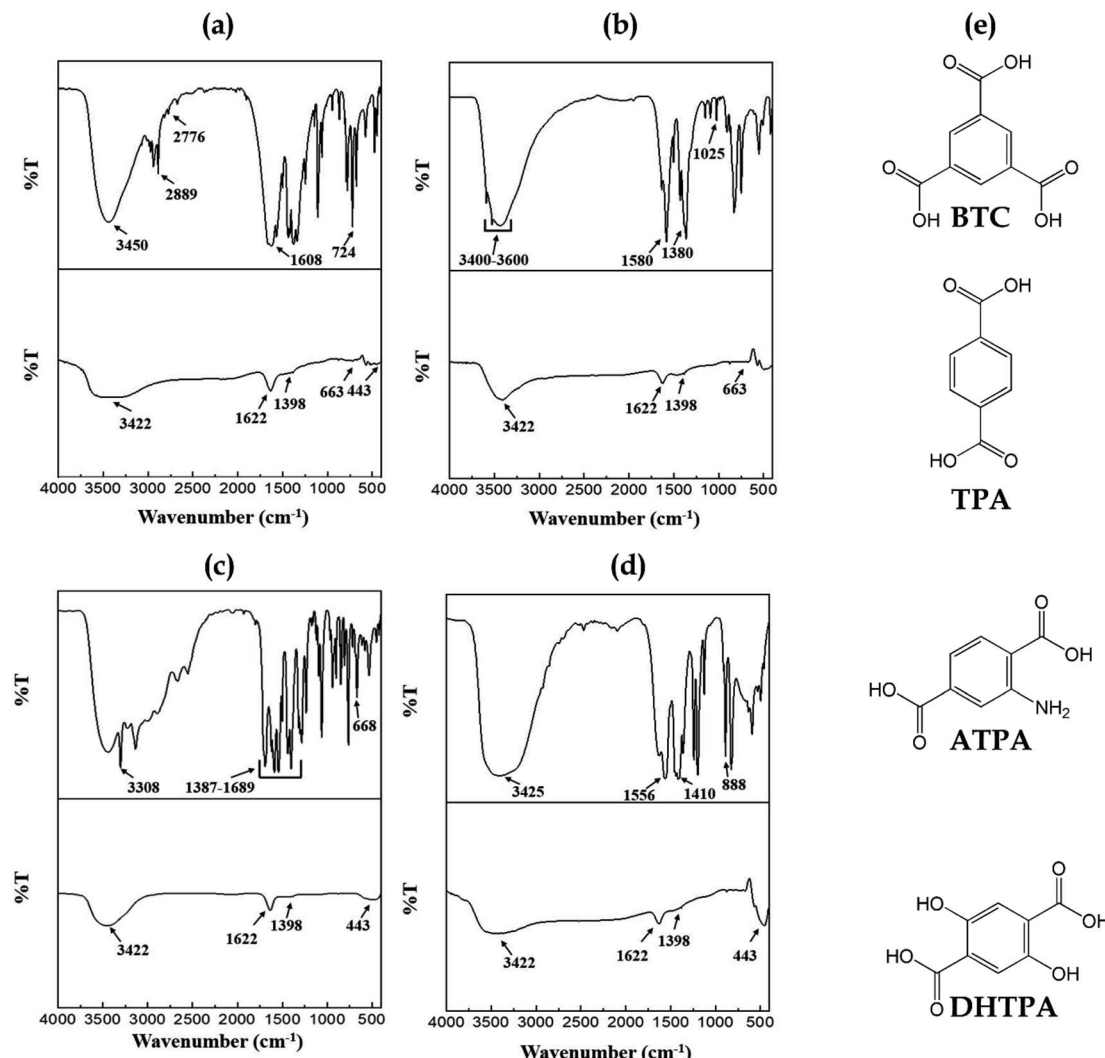


Fig. 3 FTIR spectral absorption of synthesized Ni-MOFs and its corresponding  $\text{NiO}_x$  NPs (a) Ni-BTC (b) Ni-TPA (c) Ni-ATPA (d) Ni-DHTPA and (e) the chemical structures of ligands.

during FTIR examination. The symmetric and asymmetric stretching of C–O and O=C=O may also be appeared with a narrow band intensity with the range between 1000–1500  $\text{cm}^{-1}$  that indicating a strong physical absorption to  $\text{CO}_2$  and  $\text{H}_2\text{O}$ .<sup>23,33</sup>

**3.1.2 Morphological properties.** To investigate the morphological characteristics of synthesized MOFs and their corresponding  $\text{NiO}_x$  nanoparticles, FeSEM images have been taken and the impacts of different sintering temperature on NPs morphology has also been thoroughly investigated. Fig. 4 shows the morphological properties of Ni-BTC MOF and its relevant NPs, calcined at 600 °C, 700 °C and 900 °C. It has been found that Ni-BTC MOF has a flat plate-like laminated structure that seems to be randomly arranged with high porosity (Fig. 4a). When Ni-BTC MOF was treated at 600 °C, 700 °C, and 900 °C, a systematic assessment of the morphological structure of the  $\text{NiO}_x$  NPs has been observed.  $\text{NiO}_x$  NPs seem to be well aggregated with small crystallite at calcination temperature of 600 °C (Fig. 4b); however, at 700 °C, a non-spherical random shape has

been found with less agglomeration (Fig. 4c). The particles are found to be clear, distinct crystal with spherical shapes at 900 °C (Fig. 4d). It is evident that the avg. size of particle is increased as the calcination temperature rise, which is consistent with Siamak Pilban Jahromi *et al.* study, they found that larger  $\text{NiO}_x$  NPs were obtained at higher temperature (500 °C) around 21.8 nm compare to lower calcination temperature (300 °C and 400 °C).<sup>34</sup>

SEM observations of the Ni-TPA MOF and relevant NPs at various sintering temperatures as illustrated in Fig. 5. Ni-TPA MOF showed hierarchical plate-like structure (Fig. 5a). NPs seem to be more compact, uniform-sized, and spherical in shape when MOF is treated at 600 °C (Fig. 5b). The well-defined nanostructures are also observed at 700 °C but the particles size is bigger than at 600 °C (Fig. 5c). For 700 °C, the nanoparticles size varied with ranging from 40 to 95 nm, whereas at 600 °C in between 25–50 nm. Particles at 900 °C have high crystallites with a spherical form, having particle sizes ranging from 85 to 130 nm (Fig. 5d).

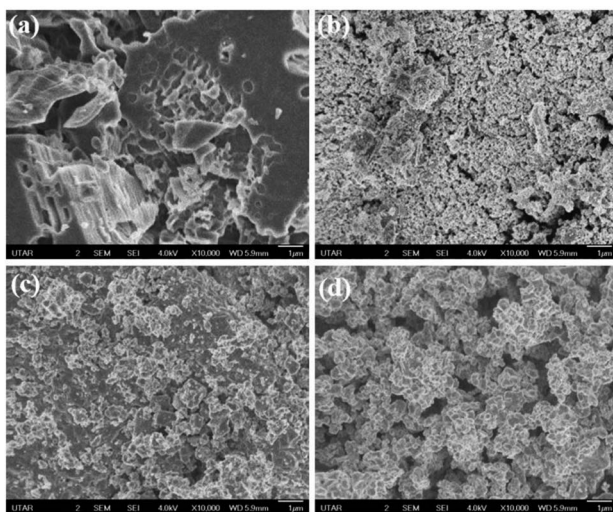


Fig. 4 FeSEM image of (a) Ni-BTC MOF and corresponding NiO<sub>x</sub> NPs calcined at (b) 600 °C (c) 700 °C (d) 900 °C.

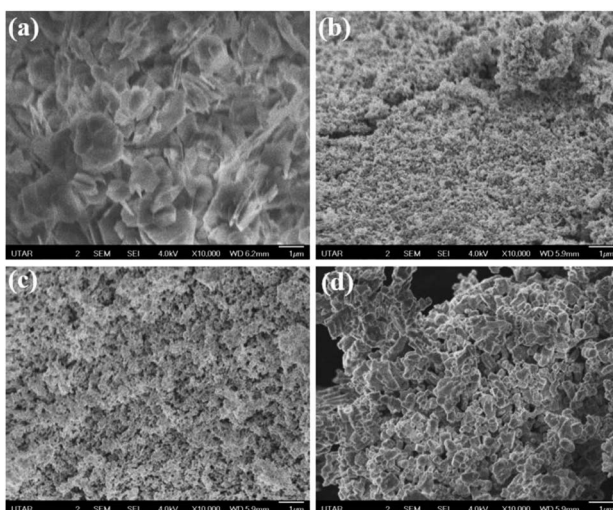


Fig. 5 FeSEM image of (a) Ni-TPA MOF and corresponding NiO<sub>x</sub> NPs calcined at (b) 600 °C (c) 700 °C (d) 900 °C.

With different calcination temperature, NiO<sub>x</sub> NPs derived from Ni-ATPA MOF exhibit the most morphological changes as shown in Fig. 6. For Ni-ATPA MOF hierarchical plate-like structure was obtained as like as Ni-TPA MOF (Fig. 6a). It has been observed that at 600 °C, the NPs are highly agglomerated and take on a spherical shape (Fig. 6b). The structure of the particle changes into a very compact reticular shape at 700 °C (Fig. 6c). Whereas at 900 °C, a quasi-cubic NPs structure has been identified (Fig. 6d).

The FeSEM image of Ni-DHTPA MOF also depicted a plate like structure (Fig. 7a). The NiO<sub>x</sub> nanoparticles exhibited an irregular shaped crystal structure for all sintering temperature; however, particle size and crystallinity improve with increasing temperatures (Fig. 7b-d).

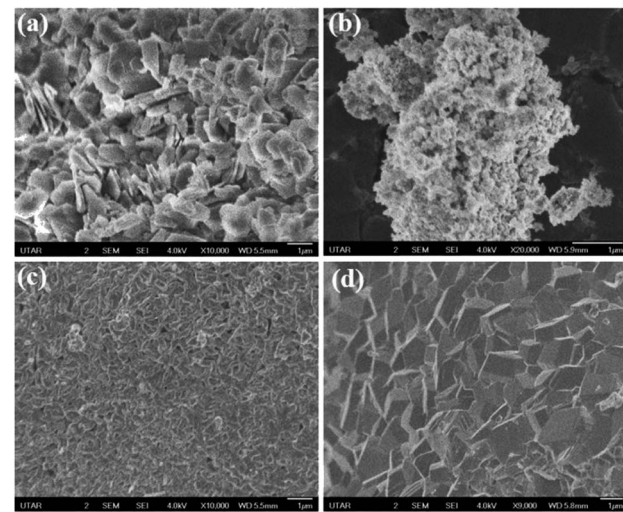


Fig. 6 FeSEM image of (a) Ni-ATPA MOF and corresponding NiO<sub>x</sub> NPs calcined at (b) 600 °C (c) 700 °C (d) 900 °C.

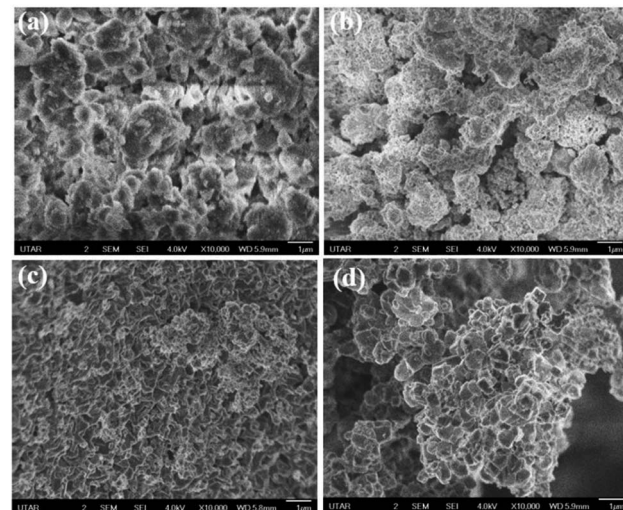


Fig. 7 FeSEM image of (a) Ni-DHTPA MOF and corresponding NiO<sub>x</sub> NPs calcined at (b) 600 °C (c) 700 °C (d) 900 °C.

**3.1.3 Optical properties.** Absorption spectra of NiO<sub>x</sub> NPs (calcined at 600 °C) derived from Ni-MOFs are shown in Fig. 8. For BTC-derived NiO<sub>x</sub> (NiO<sub>x</sub>-BTC) NPs, a strong absorption peak has been found at around 335 nm (Fig. 8a). This absorbance is the result of an electronic transition from the valence band (V<sub>B</sub>) to the conduction band (C<sub>B</sub>) in NiO<sub>x</sub> NPs.<sup>35</sup> For TPA-derived NiO<sub>x</sub> (NiO<sub>x</sub>-TPA) nanoparticles a band observed at 355 nm which is identical to previous observed value (Fig. 8b).<sup>36</sup> Absorption spectrum moves towards the shorter wavelength area (hypsochromic shift) when the NPs derived from Ni-ATPA and Ni-DHTPA MOF (Fig. 8c and d). For both NiO<sub>x</sub>-ATPA and NiO<sub>x</sub>-DHTPA, spectral band observed at the same region around 280 nm. The movement of absorptions towards a shorter wavelength may be induced by the reduction in particle size.<sup>37</sup>



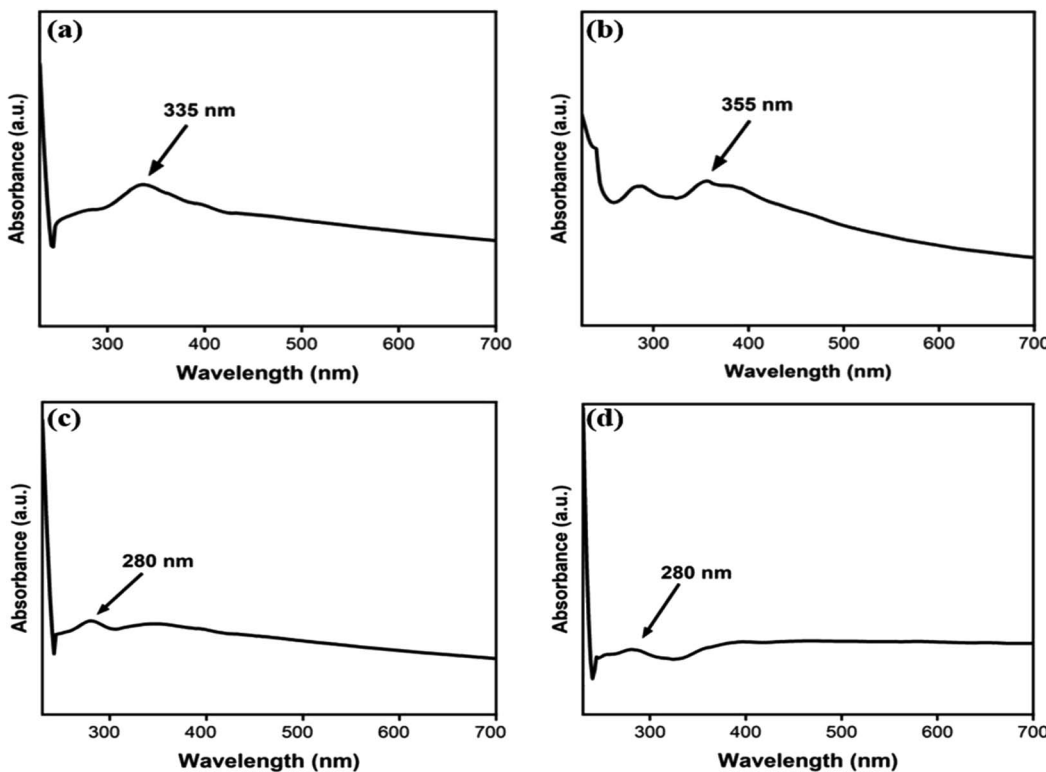


Fig. 8 UV-Visible spectra (a)  $\text{NiO}_x$ -BTC (b)  $\text{NiO}_x$ -TPA (c)  $\text{NiO}_x$ -ATPA (d)  $\text{NiO}_x$ -DHTPA nanoparticles.

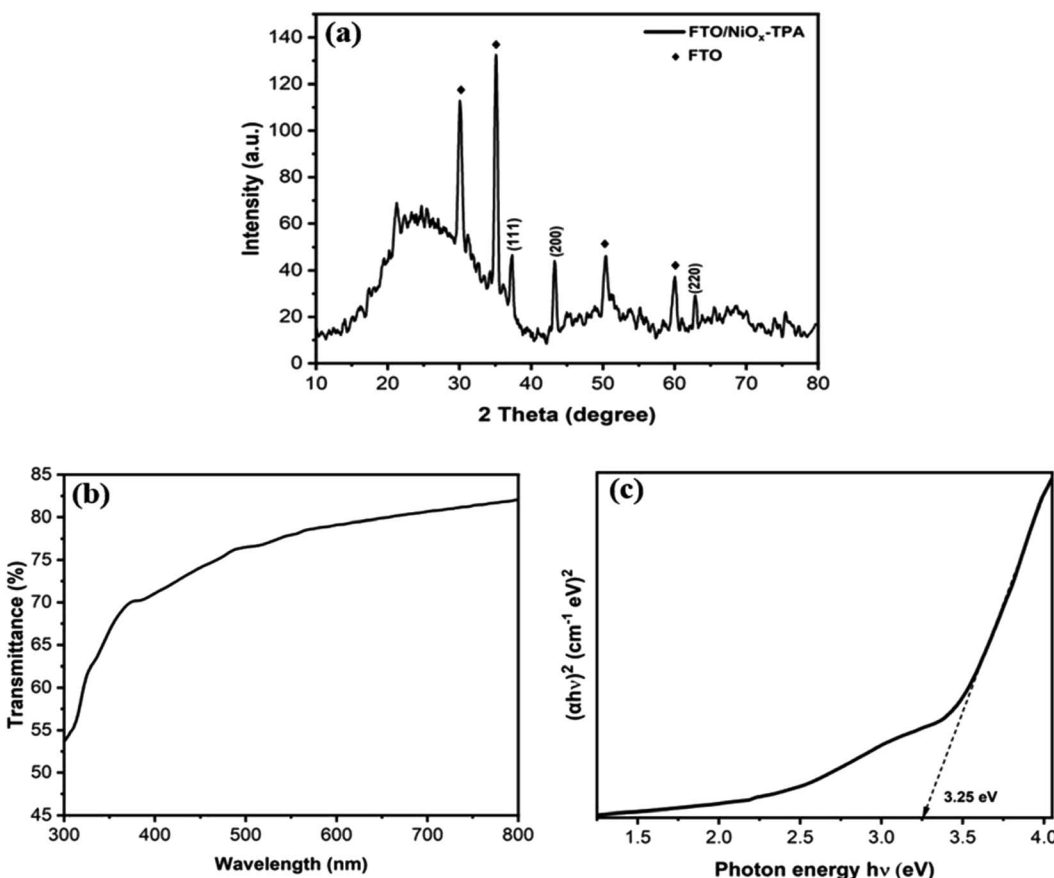


Fig. 9 Deposited  $\text{NiO}_x$  thin film's (a) XRD spectrum, (b) % of transmittance (c) Tauc plot.

### 3.2 MOF derived $\text{NiO}_x$ thin film as a potential hole transport layer (HTL) in perovskite solar cell

For the fabrication of  $\text{NiO}_x$  thin film as hole transport layer, it is important to ensure the material has small particle size with homogeneous distribution. Based on morphological properties discussed in previous section, TPA-derived  $\text{NiO}_x$  NPs calcined at 600 °C was selected for fabrication of  $\text{NiO}_x$  thin film. Fig. 9a depicts the XRD analysis of the  $\text{NiO}_x$  film deposited on the top of the FTO. The diffraction intensity for the  $\text{NiO}_x$  film have been detected at  $2\theta$  with the value of 37.0°, 43.2°, and 62.8°, which correspond to the crystallographic plane of (111), (200), and (220), respectively [JCPDS No. 73-1519]. The obtained patterns suggest a cubic phase structure, which is consistent with earlier findings.<sup>38</sup> The percentage of transmittance spectra for  $\text{NiO}_x$  thin film has been shown in Fig. 9b. In the visible spectrum region, the film had a high degree of transmittance with the values above 70% for the wavelength of 400 nm to

550 nm. The band gap ( $E_g$ ) of the thin film was calculated using Tauc plot, as shown in Fig. 9c, and found to be approximately 3.25 eV. The following equation has been employed to calculate the value of  $E_g$ :<sup>39</sup>

$$(\alpha h\nu)^{\frac{1}{n}} = A(h\nu - E_g) \quad (3)$$

where,  $E_g$  stands for the band gap;  $A$  is the constant and  $h\nu$  represents the photon energy.

Furthermore, Hall measurements were conducted to determine the carrier concentration, mobility, and resistivity of the deposited thin film. Table 2 represents the findings.

To evaluate the photovoltaic performance of TPA derived  $\text{NiO}_x$  thin film, a simulation was performed by using the SCAPS-1D software with a standard spectrum of AM1.5 G (1000 W m<sup>-2</sup>;  $T = 300$  K) for illumination. In this simulation, synthesized  $\text{NiO}_x$ -TPA (600 °C) has been used as a hole transport layer (HTL) and  $\text{TiO}_2$  ( $E_g = 3.2$  eV) as an electron transport layer (ETL).

Table 2 Hall measurement of deposited  $\text{NiO}_x$  thin film

Carrier concentration ( $\text{cm}^{-3}$ )	Resistivity ( $\Omega \text{ cm}$ )	Hole mobility ( $\text{cm}^2 \text{ V}^{-1} \text{ s}^{-1}$ )
$6.8 \times 10^{14}$ (p-type)	$4.69 \times 10^3$	2

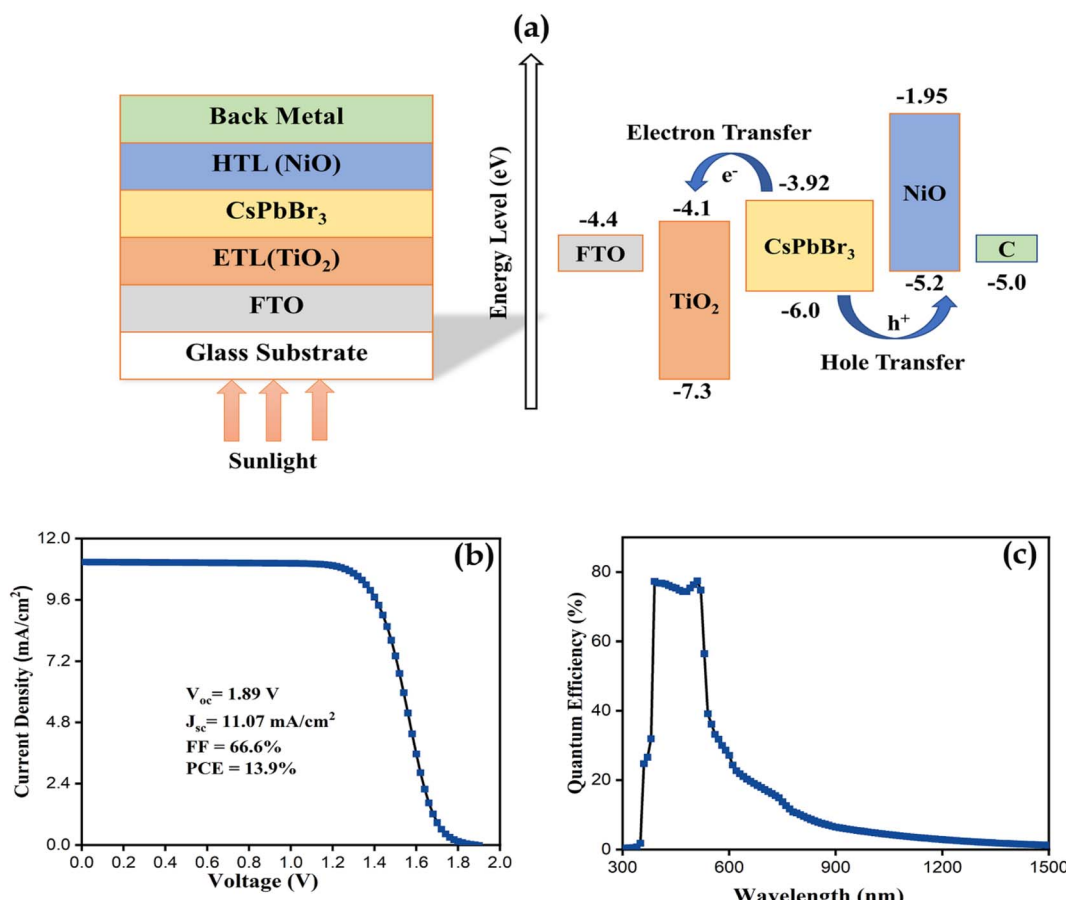


Fig. 10 (a) Schematic illustration of proposed solar structure and its band energy alignment (b)  $J$ – $V$  characteristic curves (c) quantum efficiency (Q.E) of simulated SC.



Table 3 Parameters used in device simulation

Parameters	FTO <sup>40</sup>	TiO <sub>2</sub> (ref. 40)	CsPbBr <sub>3</sub> (ref. 40)	NiO <sub>x</sub>
$W$ (nm)	200	100	300	50
$E_g$ (eV)	3.5	3.2	2.3	3.25 (exp.)
$\chi$ (eV)	4	4	3.6	1.8 (ref. 40)
$\epsilon_r$	9	9	6.5	11.75 (ref. 40)
$N_C$ (cm <sup>-3</sup> )	$2.2 \times 10^{17}$	$2.2 \times 10^{18}$	$4.94 \times 10^{17}$	$2 \times 10^{18}$ (ref. 40)
$N_V$ (cm <sup>-3</sup> )	$2.2 \times 10^{16}$	$1.8 \times 10^{19}$	$8.47 \times 10^{18}$	$2 \times 10^{18}$ (ref. 40)
$V_{th} e^-$ (cm s <sup>-1</sup> )	$1 \times 10^7$	$1 \times 10^7$	$1 \times 10^7$	$1 \times 10^7$
$V_{th} p$ (cm s <sup>-1</sup> )	$1 \times 10^7$	$1 \times 10^7$	$1 \times 10^7$	$1 \times 10^7$
$\mu_e$ (cm <sup>2</sup> V <sup>-1</sup> s <sup>-1</sup> )	$2 \times 10^1$	$2 \times 10^1$	$4.5 \times 10^3$	8
$\mu_p$ (cm <sup>2</sup> V <sup>-1</sup> s <sup>-1</sup> )	$1 \times 10^1$	$1 \times 10^1$	$4.5 \times 10^3$	2 (exp.)
$N_A$ (cm <sup>-3</sup> )	—	—	—	$6.8 \times 10^{14}$ (exp.)
$N_D$ (cm <sup>-3</sup> )	$1 \times 10^{20}$	$2 \times 10^{19}$	$1 \times 10^5$	— <sup>40</sup>

CsPbBr<sub>3</sub> employed as a perovskite with a band gap of 3.6 eV. The suggested device architecture of (FTO/TiO<sub>2</sub>/CsPbBr<sub>3</sub>/NiO<sub>x</sub>/C) has been depicted schematically in Fig. 10a. Table 3 contains a summary of the simulation parameters as shown in below.

$J$ - $V$  characteristics and quantum efficiency (Q.E) curves have been depicted in Fig. 10b and c, respectively. From the  $J$ - $V$  measurements we observed the PCE of 13.9% ( $J_{sc}$  of 11.07 mA cm<sup>-2</sup>,  $V_{oc}$  of 1.89 V, FF of 66.6%) for proposed solar cell (SC). Quantum efficiency (Q.E) for simulated solar cell showing a high quantum efficiency at visible region ranging from

390 nm to 530 nm, which is indicated to a considerable optical characteristics of proposed SC.

Literature study indicated that, Ruxin Guo *et al.* reported an efficiency of 11.21% by introducing an ionic liquid (DTPT) into CsPbBr<sub>3</sub>-based solar cell (SC) and that is the maximum PCE value ever recorded experimentally for CsPbBr<sub>3</sub>-based SC.<sup>41</sup>

In 2018, Haiwen Yuan *et al.* implanted NiO<sub>x</sub> as hole transporting material in CsPbBr<sub>3</sub>-based SC and obtained a PCE of 7.29%.<sup>42</sup> Most recently, Yu Zou *et al.* also fabricated a CsPbBr<sub>3</sub>-photovoltaic device with incorporating NiO<sub>x</sub> nano-crystal thin

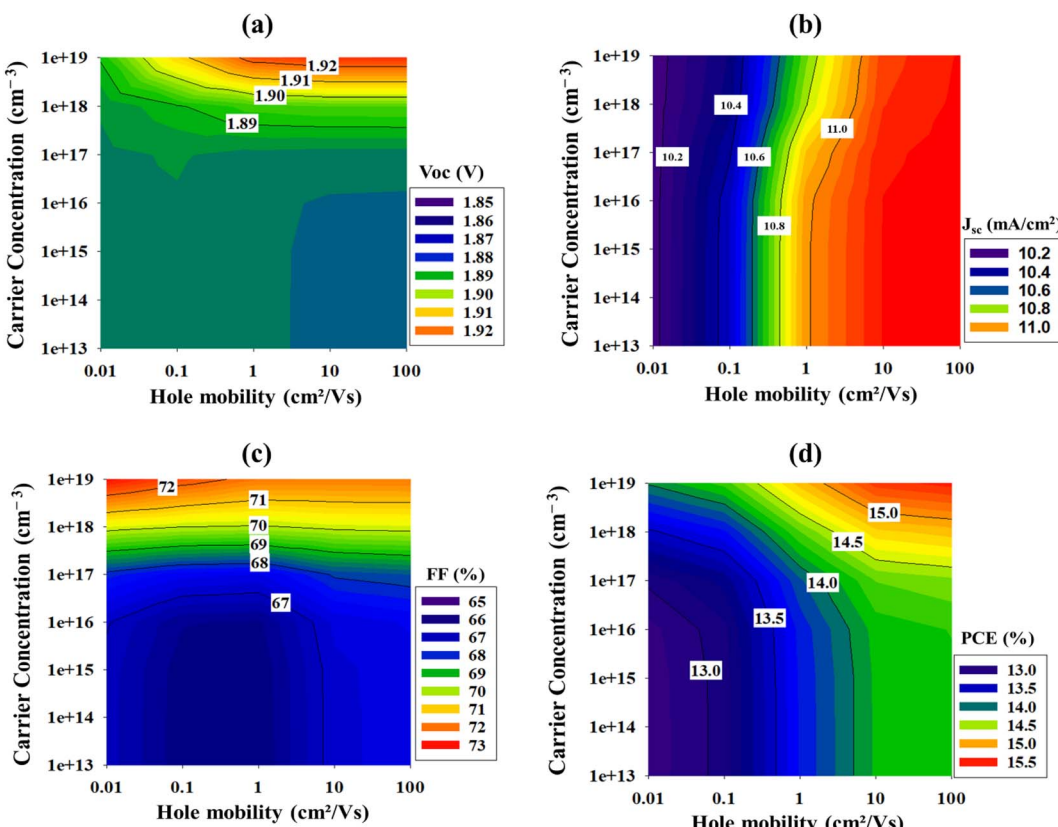


Fig. 11 (a) Performance parameters of CsPbBr<sub>3</sub> solar cell with different carrier concentration ( $\rho$ ) and hole mobility ( $\mu_p$ ) of NiO<sub>x</sub> HTL layer (a)  $\mu_p$  vs.  $\rho$  vs.  $V_{oc}$  (b)  $\mu_p$  vs.  $\rho$  vs.  $J_{sc}$  (c)  $\mu_p$  vs.  $\rho$  vs. FF (%) (d)  $\mu_p$  vs.  $\rho$  vs. PCE (%).



Table 4 Comparative analysis of electrical properties of deposited  $\text{NiO}_x$  thin film with the previously published literature

$\text{NiO}_x$ thin film	Carrier concentration ( $\text{cm}^{-3}$ )	Hole mobility ( $\text{cm}^2 \text{V}^{-1} \text{s}^{-1}$ )	References
Boric acid mediated (BA)- $\text{NiO}_x$	$2.17 \times 10^{19}$	$5.35 \times 10^{-2}$	46
$\text{NiO}_x$	$4.08 \times 10^{18}$	$2.41 \times 10^{-2}$	46
Fe- $\text{NiO}_x$	$3.331 \times 10^{12}$	6.22	47
$\text{NiO}_x$	$1.93 \times 10^{12}$	2.60	47
Cu- $\text{NiO}_x$	$2.16 \times 10^{16}$	$40 \times 10^{-2}$	48
$\text{NiO}_x$	$1.50 \times 10^{16}$	$14 \times 10^{-2}$	48
$\text{NiO}_x$	$1.37 \times 10^{17}$	$1.32 \times 10^{-3}$	49
TPA-derived $\text{NiO}_x$	$6.8 \times 10^{14}$	2	This work

film and enhanced the efficiency at around 9.19%.<sup>43</sup> In order to investigate the potential of  $\text{NiO}_x$  as a HTL layer in  $\text{CsPbBr}_3$ -based SC, a numerical simulation was carried out to elucidate the combinatorial effects of carrier concentration and hole mobility of  $\text{NiO}_x$  thin film on the overall photovoltaic performance parameters of  $\text{CsPbBr}_3$  device.

Fig. 11, illustrates the performance parameters of simulated  $\text{CsPbBr}_3$  solar cell with different carrier concentration and hole mobility of  $\text{NiO}_x$  HTL layer. To investigate the influence of HTL carrier concentration ( $p$ ) and hole mobility ( $\mu_p$ ) on device performances,  $p$  and  $\mu_p$  were varied from  $1 \times 10^{13} \text{ cm}^{-3}$  to  $1 \times 10^{19} \text{ cm}^{-3}$  and  $0.001 \text{ cm}^2 \text{ V}^{-1} \text{ s}^{-1}$  to  $100 \text{ cm}^2 \text{ V}^{-1} \text{ s}^{-1}$ , respectively. According to Fig. 11, the maximum values of  $p$  ( $1 \times 10^{19} \text{ cm}^{-3}$ ) and  $\mu_p$  ( $100 \text{ cm}^2 \text{ V}^{-1} \text{ s}^{-1}$ ) provide the highest PCE value at around 15.44% for simulated device. The reason of the increment in PCE value is due to fact that, when  $p$  rises HTL's internal electric field also rises, causing an increase in charge conductivity and transport velocity.<sup>44</sup> On the other hand, an increment in hole mobility ( $\mu_p$ ) will increase the diffusion length of charge carriers, that will make it easier to transport charge carriers without large amount of recombination and subsequently resulting higher PCE value.<sup>45</sup> Table 4 below shows the carrier concentration and hole mobility of  $\text{NiO}_x$  thin film from the various previous works, as well as the values obtained from this study.

By comparing the results from Fig. 11 and Table 4, it is evident that, there exist a large room for improvement in both carrier concentration and hole mobility parameters of  $\text{NiO}_x$  thin film that needs to be implemented, if the current record efficiency of  $\text{CsPbBr}_3$  solar cell is to be surpassed.

## 4 Conclusions

In this work, MOF derived  $\text{NiO}_x$  nanoparticles were synthesized by utilizing four distinct ligands (BTC/TPA/ATPA/DHTPA). A comparative investigation on the structural, morphological and optical properties of the MOF-derived synthesized NPs have been carried out. The findings of the FeSEM analysis demonstrate that the synthesized  $\text{NiO}_x$  NPs have variable morphological structure, depending on the ligand of MOFs as well as with the calcination temperature. From the FeSEM, it was observed that, the TPA-derived  $\text{NiO}_x$  exhibited relatively a small particle size (25–50 nm) with homogenous distribution compare to others, where ATPA derived  $\text{NiO}_x$  NPs showed the most

significant morphological changes. The fabrication of  $\text{NiO}_x$ -thin film was also carried out by employing TPA-derived  $\text{NiO}_x$  ( $600^\circ \text{C}$ ). The structural, optical and electrical characteristics of the thin film have also been studied, where thin film showing a cubic phase structure with the band gap of 3.25 eV. Carrier concentration, hole mobility and resistivity were measured to be  $6.8 \times 10^{14} \text{ cm}^{-3}$ ;  $4.7 \times 10^{14} \Omega \text{ cm}$  and  $2.0 \text{ cm}^2 \text{ V}^{-1} \text{ s}^{-1}$ , respectively. A numerical simulation was also performed to investigate the photovoltaic performance of the TPA-derived  $\text{NiO}_x$  thin film. The efficiency of the device was measured at around 13.9% with the  $J_{sc}$  of  $11.07 \text{ mA cm}^{-2}$ ,  $V_{oc}$  of  $1.89 \text{ V}$  and FF of 66.6%.

## Conflicts of interest

There are no conflicts to declare.

## Acknowledgements

We appreciate the Universiti Kebangsaan Malaysia (UKM) (@The National University of Malaysia) for the financial assistance through the SRF – APP MIMOS UKM grant (RS-2021-003). The authors extend their appreciation to Researchers Supporting Project number (RSP2023R34), King Saud University, Riyadh, Saudi Arabia. The authors also gratefully acknowledge Dr Marc Burgelman, University of Gent, Belgium, for providing the SCAPS- 1D simulation software.

## References

- Y. Wu, Y. He, T. Wu, T. Chen, W.-z. Weng and H.-L. Wan, *Mater. Lett.*, 2007, **61**, 3174–3178.
- K. Anandan and V. Rajendran, *Mater. Sci. Semicond. Process.*, 2011, **14**, 43–47.
- M.-S. Wu and Y.-P. Lin, *Electrochim. Acta*, 2011, **56**, 2068–2073.
- Y. Wang, J. Zhu, X. Yang, L. Lu and X. Wang, *Thermochim. Acta*, 2005, **437**, 106–109.
- Y.-Z. Zheng and M.-L. Zhang, *Mater. Lett.*, 2007, **61**, 3967–3969.
- A. Aslani, V. Oroojpour and M. Fallahi, *Appl. Surf. Sci.*, 2011, **257**, 4056–4061.
- A. C. Johnston-Peck, J. Wang and J. B. Tracy, *ACS Nano*, 2009, **3**, 1077–1084.



8 J. Bandara, C. M. Divarathne and S. D. Nanayakkara, *Sol. Energy Mater. Sol. Cells*, 2004, **81**, 429–437.

9 R. Kaneko, H. Kanda, K. Sugawa, J. Otsuki, A. Islam and M. K. Nazeeruddin, *Sol. RRL*, 2019, **3**, 1900172.

10 X. Wang, J. Song, L. Gao, J. Jin, H. Zheng and Z. Zhang, *Nanotechnology*, 2005, **16**, 37.

11 P. Justin, S. K. Meher and G. R. Rao, *J. Phys. Chem. C*, 2010, **114**, 5203–5210.

12 Y.-H. Seo, I. H. Cho and S.-I. Na, *J. Alloys Compd.*, 2019, **797**, 1018–1024.

13 P.-H. Lee, T.-T. Wu, C.-F. Li, D. Głowienka, Y.-H. Sun, Y.-T. Lin, H.-W. Yen, C.-G. Huang, Y. Galagan, Y.-C. Huang and W.-F. Su, *Chem. Eng. J.*, 2021, **412**, 128746.

14 S. Wang, Y. Li, J. Yang, T. Wang, B. Yang, Q. Cao, X. Pu, L. Etgar, J. Han, J. Zhao, X. Li and A. Hagfeldt, *Angew. Chem., Int. Ed.*, 2022, **61**, e202116534.

15 S. Pilban Jahromi, N. M. Huang, M. R. Muhamad and H. N. Lim, *Ceram. Int.*, 2013, **39**, 3909–3914.

16 G. Thangamani J., K. Deshmukh, B. Ahamed, K. Chidambaram, K. Saranya and S. Pasha, *Int. J. ChemTech Res.*, 2015, **8**, 974–4290.

17 Y. Sun and H.-C. Zhou, *Sci. Technol. Adv. Mater.*, 2015, **16**, 054202.

18 D. Y. Heo, H. H. Do, S. H. Ahn and S. Y. Kim, *Polymers*, 2020, **12**, 2061.

19 L. Pan, T. Muhammad, L. Ma, Z.-F. Huang, S. Wang, L. Wang, J.-J. Zou and X. Zhang, *Appl. Catal., B*, 2016, **189**, 181–191.

20 T. Prabhakaran, R. V. Mangalaraja, J. C. Denardin and J. A. Jiménez, *J. Alloys Compd.*, 2017, **716**, 171–183.

21 N. C. Horti, M. D. Kamatagi, S. K. Nataraj, M. N. Wari and S. R. Inamdar, *Nano Express*, 2020, **1**, 010022.

22 S. Suresh and J. Podder, *Int. J. Nanopart.*, 2015, **8**, 289–301.

23 Q. Hongxia, W. Zhiqiang, Y. Hua, Z. Lin and Y. Xiaoyan, *J. Nanomater.*, 2009, 479.

24 V. Selvanathan, M. Shahinuzzaman, S. Selvanathan, D. K. Sarkar, N. Algethami, H. I. Alkhammash, F. H. Anuar, Z. Zainuddin, M. Aminuzzaman, H. Abdulla and M. Akhtaruzzaman, *Catalysts*, 2021, **11**, 1523.

25 N. Saikumari, S. M. Dev and S. A. Dev, *Sci. Rep.*, 2021, **11**, 1734.

26 T. Sinha, L. Verma and A. Khare, *Appl. Phys. A: Mater. Sci. Process.*, 2020, **126**, 867.

27 W. W. Lestari, I. D. Winarni and F. Rahmawati, *IOP Conf. Ser.: Mater. Sci. Eng.*, 2017, **172**, 012064.

28 F. Wang, X. Chen, L. Chen, J. Yang and Q. Wang, *Mater. Sci. Eng., C*, 2019, **96**, 41–50.

29 R. Salama, S. Abd El-Hakam, S. Samra, S. El-dafrawy and A. Ahmed, *Int. J. Mod. Chem.*, 2018, **20**(10), 195–207.

30 S. Yang, J. Zhang, C. Bai and K. Deng, *Can. J. Chem.*, 2020, **99**, 465–473.

31 Y. Liao, C. Li, X. Lou, P. Wang, Q. Yang, M. Shen and B. Hu, *J. Colloid Interface Sci.*, 2017, **506**, 365–372.

32 J.-J. Song, B. He, X. Wang, Y. Guo, C. Peng, Y. Wang, Z. Su and Q. Hao, *J. Mater. Sci.*, 2021, **56**, 17178–17190.

33 S. D. Khairnar and V. S. Shrivastava, *J. Taibah Univ. Sci.*, 2019, **13**, 1108–1118.

34 S. Pilban Jahromi, A. Pandikumar, B. T. Goh, Y. S. Lim, W. J. Basirun, H. N. Lim and N. M. Huang, *RSC Adv.*, 2015, **5**, 14010–14019.

35 Z. Sabouri, N. Fereydouni, A. Akbari, H. A. Hosseini, A. Hashemzadeh, M. S. Amiri, R. Kazemi Oskouee and M. Darroudi, *Rare Met.*, 2020, **39**, 1134–1144.

36 A. Barakat, M. Al-Noaimi, M. Suleiman, A. S. Aldwayyan, B. Hammouti, T. B. Hadda, S. F. Haddad, A. Boshala and I. Warad, *Int. J. Mol. Sci.*, 2013, **14**, 23941–23954.

37 S.-J. Hong, H.-J. Mun, B.-J. Kim and Y.-S. Kim, *Micromachines*, 2021, **12**, 1168.

38 Z.-W. Huang, S.-H. Yang, Z.-Y. Wu and H.-C. Hsu, *ACS Omega*, 2021, **6**, 15855–15866.

39 S. Jana, G. Mondal, B. C. Mitra, P. Bera, B. Chakraborty, A. Mondal and A. Ghosh, *New J. Chem.*, 2017, **41**, 14985–14994.

40 S. Rani, D. Kuar, V. Jeyachandran and D. S. Ghosh, *Opt. Mater.*, 2022, **131**, 112612.

41 R. Guo, J. Xia, H. Gu, X. Chu, Y. Zhao, X. Meng, Z. Wu, J. Li, Y. Duan, Z. Li, Z. Wen, S. Chen, Y. Cai, C. Liang, Y. Shen, G. Xing, W. Zhang and G. Shao, *J. Mater. Chem. A*, 2023, **11**, 408–418.

42 H. Yuan, Y. Zhao, J. Duan, Y. Wang, X. Yang and Q. Tang, *J. Mater. Chem. A*, 2018, **6**, 24324–24329.

43 Y. Zou, F. Cao, P. Chen, R. He, A. Tong, C. Yin, Z. Lan, W. Sun and J. Wu, *Electrochim. Acta*, 2022, **435**, 141392.

44 G. Pindolia, S. M. Shinde and P. K. Jha, *Sol. Energy*, 2022, **236**, 802–821.

45 C. Pinzón, N. Martínez, G. Casas, F. C. Alvira, N. Denon, G. Brusasco, H. Medina Chanduví, A. V. Gil Rebaza and M. A. Cappelletti, *Solar*, 2022, **2**, 559–571.

46 B. Ge, Z. Q. Lin, Z. R. Zhou, H. W. Qiao, A. P. Chen, Y. Hou, S. Yang and H. G. Yang, *Sol. RRL*, 2021, **5**, 2000810.

47 P. S. Chandrasekhar, Y.-H. Seo, Y.-J. Noh and S.-I. Na, *Appl. Surf. Sci.*, 2019, **481**, 588–596.

48 M. Feng, M. Wang, H. Zhou, W. Li, S. Wang, Z. Zang and S. Chen, *ACS Appl. Mater. Interfaces*, 2020, **12**, 50684–50691.

49 X. Jin, Y. Yuan, C. Jiang, H. Ju, G. Jiang, W. Liu, C. Zhu and T. Chen, *Sol. Energy Mater. Sol. Cells*, 2018, **185**, 542–548.

